Article

Square-root higher-order Weyl semimetals

Lingling Song [1], Huanhuan Yang [1], Yunshan Cao[1] & Peng Yan [1] ✉

The mathematical foundation of quantum mechanics is built on linear algebra, while the application of nonlinear operators can lead to outstanding discoveries under some circumstances, such as the prediction of positron, a direct outcome of the Dirac equation which stems from the square-root of the Klein-Gordon equation. In this article, we propose a model of square-root higher-order Weyl semimetal (SHOWS) by inheriting features from its parent Hamiltonians. It is found that the SHOWS hosts both "Fermi-arc" surface and hinge states that respectively connect the projection of the Weyl points on the side surface and arris. We theoretically construct and experimentally observe the exotic SHOWS state in three-dimensional (3D) stacked electric circuits with honeycomb-kagome hybridizations and double-helix interlayer couplings. Our results open the door for realizing the square-root topology in 3D solid-state platforms.

Nearly all the operators encountered in quantum mechanics are linear (or antilinear) operators, such as the rotation, translation, parity, time reversal, etc, which allows us to construct the mathematical basis of quantum mechanics formulated on linear algebra. Square-root operator is one of the few exceptions. Historically, Paul Dirac derived the Dirac equation through a square-root operation on the Klein-Gordon (KG) equation to describe all spin-$\frac{1}{2}$ massive particles that inherit the Lorentz-covariance of the parent KG equation[1–3]. The approach has inspired Arkinstall et al.[4] to propose the concept of square-root topological insulator (TI) by taking the nontrivial square-root of a tight-binding (TB) Hamiltonian in periodic lattices. The most appealing feature of square-root TI is that it inherits the nontrivial nature of Bloch wave function from its parent Hamiltonian. The square-root TI was subsequently observed in a photonic cage[5]. Recently, the square-root operation has been applied to higher-order topological insulators (HOTIs) that allow topologically robust edge states with codimension larger than one[6–16]. Besides the gapped solution, e.g., the electron-positron pair, the Dirac equation allows another crucial gapless or massless solution called Weyl fermion[17] that plays an important role in quantum field theory and the standard Model. Although not yet observed among elementary particles, Weyl fermions are shown to exist as collective excitations in Weyl semimetals[18–21]. For the conventional Weyl semimetal, the three-dimensional (3D) topology features two-dimensional (2D) gapped surface states that connect the projection of Weyl points on the surface[18–21]. Very recently,

higher-order Weyl semimetal was reported which supports both the 2D surface Fermi arcs and the one-dimensional (1D) hinge state[22–29]. It is thus intriguing to ask if the square-root operation can apply to semimetals[30] or higher-order semimetals, and particularly how to realize these exotic states in experiments.

In this article, we propose a TB model of the square-root higher-order Weyl semimetal (SHOWS) by a vertical stacking of 2D square-root HOTIs with interlayer couplings in a double-helix fashion. It is found that the SHOWS hosts both 2D surface arc states and 1D hinge states with the topological feature being fully characterized by the quantized bulk polarization or edge invariant. We construct the TB model in stacked honeycomb-kagome (HK) hybridized inductor-capacitor (LC) circuit networks. By performing both the impedance and voltage measurements, we identify the fingerprint of the SHOWS by directly observing the Weyl points, the "Fermi arc" surface states, and the hinge states. It is revealed that both the surface states and the hinge states ideally connect the projections of the Weyl points on side surface and arris respectively, consistent with theoretical calculations.

Results
Model
Figure 1a shows the lattice structure of the proposed model, the square of which can be viewed as the direct sum of a stacked honeycomb and a breathing kagome lattices (Fig. 1b and the analysis in

[1]School of Electronic Science and Engineering and State Key Laboratory of Electronic Thin Films and Integrated Devices, University of Electronic Science and Technology of China, Chengdu 610054, China. ✉e-mail: yan@uestc.edu.cn
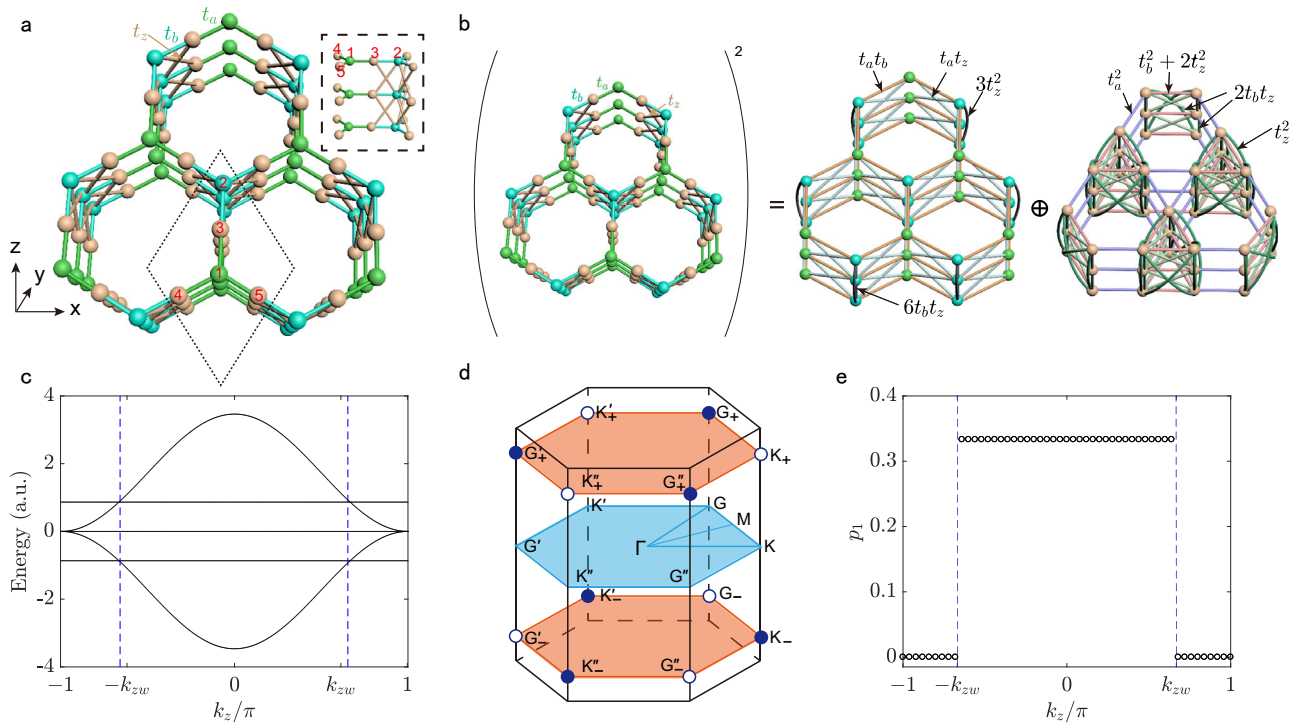
Fig. 1 | 3D stacked HK TB model. a Illustration of an infinite 3D stacked HK TB model. The unit cell including five nodes is represented by the dashed black rhombus. The intralayer hoppings are t_a and t_b (blue) in the $x - y$ plane, whereas the interlayer double-helix hopping is t_z (brown). Insets: Right view of the cell. **b** The equivalence between the squared Hamiltonian of the HK circuit and its parents. **c** The bulk dispersion along the k_z direction with $(k_x, k_y) = (4\pi/3, 0)$. The dashed blue line indicates the position of the degenerate points. **d** The first Brillouin zone and the distribution of the Weyl points. The hallow and solid circles represent the Weyl point with the charge ± 1. **e** Bulk polarization p_1 as a function of k_z. For TB calculations in **c** and **e**, we set $t_a = 0.5$, $t_b = 1$, and $t_z = 0.5$.

Supplementary Note 1). The TB Hamiltonian is given by

$$\mathcal{H} = t_a \sum_{\langle m,n \rangle} \left(a_m^\dagger c_n + a_m^\dagger d_n + a_m^\dagger e_n \right)$$
$$+ t_b \sum_{\langle m,n \rangle} \left(b_m^\dagger c_n + b_m^\dagger d_n + b_m^\dagger e_n \right) \qquad (1)$$
$$+ t_z \sum_{\langle\langle m,n \rangle\rangle} \left(b_m^\dagger c_n + b_m^\dagger d_n + b_m^\dagger e_n \right) + \text{H.c.},$$

where $a^\dagger (a)$, $b^\dagger (b)$, $c^\dagger (c)$, $d^\dagger (d)$, and $e^\dagger (e)$ are the creation (annihilation) operators on the site 1-5, respectively, $\langle m, n \rangle$ and $\langle\langle m, n \rangle\rangle$ label the nearest-neighbor and next-nearest-neighbor coupling, respectively, and t_a, t_b, and t_z are the hopping parameters. H.c. represents the Hermitian conjugate. In Fig. 1a, the nearest-neighbor sites of node 1(2) are nodes 3,4,5 with t_a, t_b being the intralayer hopping parameters. The next-nearest-neighbor sites of node 2 are nodes 2, 3 and 4 in the adjacent layer with t_z being the interlayer hopping parameter. Without loss of generality, we assume all hopping paramaters are positive. In momentum space, the Hamiltonian can be expressed as

$$\mathcal{H} = \begin{pmatrix} O_{2,2} & \Phi_{\mathbf{k}}^\dagger \\ \Phi_{\mathbf{k}} & O_{3,3} \end{pmatrix}, \qquad (2)$$

where $O_{2,2}$ and $O_{3,3}$ are the 2×2 and 3×3 zero matrix, respectively, and $\Phi_{\mathbf{k}}$ is the 3×2 matrix

$$\Phi_{\mathbf{k}} = \begin{pmatrix} t_a & t_b + 2t_z \cos(\mathbf{k} \cdot \mathbf{a}_3) \\ t_a & [t_b + 2t_z \cos(\mathbf{k} \cdot \mathbf{a}_3)]e^{-i\mathbf{k} \cdot \mathbf{a}_1} \\ t_a & [t_b + 2t_z \cos(\mathbf{k} \cdot \mathbf{a}_3)]e^{-i\mathbf{k} \cdot \mathbf{a}_2} \end{pmatrix}. \qquad (3)$$

Here $\mathbf{k} = (k_x, k_y, k_z)$ is the wave vector, and $\mathbf{a}_1 = \frac{1}{2}\hat{x} + \frac{\sqrt{3}}{2}\hat{y}$, $\mathbf{a}_2 = -\frac{1}{2}\hat{x} + \frac{\sqrt{3}}{2}\hat{y}$ and $\mathbf{a}_3 = \hat{z}$ are three basic vectors.

By taking the square of the original Hamiltonian (2), we can conveniently obtain the dispersion relation of $[\mathcal{H}]^2$ (see Supplementary Note 1)

$$E_{\mathbf{k}} = 0 \quad \text{and} \quad \frac{3}{2}\left[t_a^2 + t_b'^2 \pm \sqrt{(t_a^2 - t_b'^2)^2 + 4t_a^2 t_b'^2 |\Delta(\mathbf{k})|^2} \right], \qquad (4)$$

with $t_b' = t_b + 2t_z \cos(k_z)$ and $\Delta(\mathbf{k}) = (1 + e^{i\mathbf{k} \cdot \mathbf{a}_1} + e^{i\mathbf{k} \cdot \mathbf{a}_2})/3$. The band structure of the original Hamiltonian is thus given by $\varepsilon_{\mathbf{k}} = \pm \sqrt{E_{\mathbf{k}}}$. It is found that the band structure closes at the twofold degenerate points $K_\pm = (4\pi/3, 0, \pm k_{zw})$, as shown in Fig. 1c, with $k_{zw} = \arccos[(t_a - t_b)/(2t_z)]$ when $|t_a - t_b| < 2t_z$. It is straightforward to verify that their time-reversal counterparts are $G_\pm' = (-4\pi/3, 0, \pm k_{zw})$, and their equivalence points locate at $G_\pm$, $G_\pm''$, $K_\pm'$, and $K_\pm''$, as shown in Fig. 1d. By evaluating the topological charge C_{FS}, we find that the hollow and solid circles plotted in Fig. 1d denote the Weyl points with opposite topological charges, i.e., $+1$ and -1, respectively (see Supplementary Fig. 1). In addition, we derive the low-energy effective Hamiltonian near the degeneracy points, and obtain a linear crossing in the vicinity of the Weyl points (Supplementary Note 2). The computation of Berry curvatures are plotted in Supplementary Fig. 1c, d, which indeed demonstrates that the Weyl points manifest as singularities (source and drain), a close analog to the magnetic monopole in momentum space.

For a system with the rotational symmetry (it is C_3 in our model), the bulk polarization is the appropriate invariant to characterize the topological features. For the nth band, the bulk polarization[7] as a
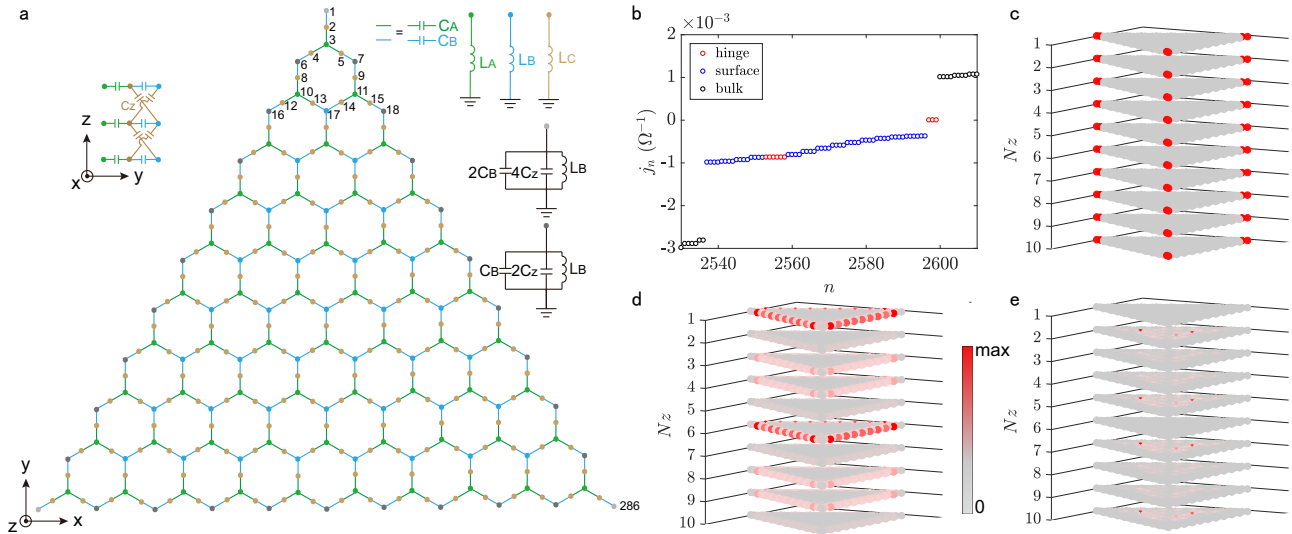
Fig. 2 | Finite-size circuit model. a Top view of a stacked 10-layer HK circuit with 2860 nodes. The green and blue segments represent the capacitors C_A and C_B, respectively, and each node is grounded by capacitors and inductors with the configurations shown in the insets. The finite-size equilateral triangular structure with the zigzag edge was chosen because one requires a uniform onsite admittance for all nodes of the breathing kagome block that appears upon squaring the Laplacian. **b** Admittances for $C_A = C_Z = C_B/2 = 0.5$ nF, $L_A = 30$ μH, $L_B = 7.5$ μH, $L_C = 18$ μH, and $L_G = 21.829$ μH. The red, blue, black symbols represent the hinge, surface, bulk states, respectively. Spatial distribution of the wave functions of the normalized hinge state ($j_n = 3.534 \times 10^{-7}\ \Omega^{-1}$) (**c**), surface state ($j_n = -0.0003762\ \Omega^{-1}$) (**d**), and bulk state ($j_n = 0.001042\ \Omega^{-1}$) (**e**).

function of k_z is written as

$$2\pi p_n(k_z) = \arg \theta_n(\mathbf{k})\,(\mathrm{mod}\ 2\pi), \tag{5}$$

where $\mathbf{k} = (4\pi/3, 0, k_z)$, and $\theta_n(\mathbf{k}) = u_n^\dagger(\mathbf{k}) U_{\mathbf{k}} u_n(\mathbf{k})$ with $u_n(\mathbf{k})$ the nth eigenvector and the U-matrix

$$U_{\mathbf{k}} = \begin{pmatrix} 1 & 0 & 0 & 0 & 0 \\ 0 & e^{-i\mathbf{k}\cdot\mathbf{a}_2} & 0 & 0 & 0 \\ 0 & 0 & 0 & 0 & 1 \\ 0 & 0 & 0 & 1 & 0 \\ 0 & 0 & 1 & 0 & 0 \end{pmatrix}. \tag{6}$$

Here we are particularly interested in the 1st (or 5th) band, because the Weyl points only appear in the intersecting between the first and second energy bands (or between the fourth and fifth energy bands). As shown in Fig. 1e, p_1 takes 1/3 for $|k_z| < |k_{zw}|$, and 0 for $|k_z| > |k_{zw}|$. The topological phase transition occurs at $k_z = \pm k_{zw}$. A non-vanishing p_1 indicates the very presence of the higher-order topological states. As a comparison, we also calculate the edge topological invariant following the method of[10,31]. We identify the same phase transition point at $\pm k_{zw}$, as shown in Supplementary Fig. 3b. The present model unambiguously demonstrates the bulk-hinge correspondence and manifests itself as an ideal SHOWS (Supplementary Fig. 2d). It is noted that a pair of Weyl points emerge with opposite wave vectors (Fig. 1c) because of the inversion-symmetry breaking in our model. It is worth mentioning that the present model also allows a 3D square-root HOTI phase (Supplementary Fig. 2e–g). Electronic circuits are an excellent platform to study topological physics[32–43]. In what follows, we construct the TB SHOWS model in 3D stacked HK LC circuits.

Circuit realization of SHOWS
We consider a stacked 10-layer HK circuit with $\mathcal{N} = 2860$ nodes, as depicted in Fig. 2a. The dots and lines represent nodes and capacitors, respectively. The circuit dynamics at frequency ω obeys Kirchhoff's law $I_a(\omega) = \sum_b J_{ab}(\omega) V_b(\omega)$, with I_a the external

current flowing into node a, V_b the voltage of node b, and $J_{ab}(\omega)$ being the circuit Laplacian

$$J(\omega) = \begin{pmatrix} J_{0B} & -J_B & 0 & \dots & 0 & -J_Z & 0 & \cdots_1 \\ -J_B & J_{0C} & -J_A & \cdots & -J_Z & 0 & 0 & \cdots_2 \\ 0 & -J_A & J_{0A} & \cdots & 0 & 0 & 0 & \cdots_3 \\ \vdots & \vdots & \vdots & \ddots & \vdots & \vdots & \vdots & \ddots \\ 0 & -J_Z & 0 & \cdots & J_{0B} & -J_B & 0 & \cdots_{287} \\ -J_Z & 0 & 0 & \cdots & -J_B & J_{0C} & -J_A & \cdots_{288} \\ 0 & 0 & 0 & \cdots & 0 & -J_A & J_{0A} & \cdots_{289} \\ \vdots_1 & \vdots_2 & \vdots_3 & \vdots & \vdots_{287} & \vdots_{288} & \vdots_{289} & \ddots \end{pmatrix} \tag{7}$$

with $J_{0A} = 3i\omega C_A - 1/(i\omega L_A)$, $J_{0B} = 3i\omega(C_B + 2C_Z) - 1/(i\omega L_B)$, $J_{0C} = i\omega(C_A + C_B + 2C_Z) - 1/(i\omega L_C)$, $J_A = i\omega C_A$, $J_B = i\omega C_B$, $J_Z = i\omega C_Z$ and the subscript of the dots indicating the column/row numbers. Under the resonance condition $\omega_0 = 1/\sqrt{3C_A L_A} = 1/\sqrt{(3C_B + 6C_Z)L_B} = 1/\sqrt{(C_A + C_B + 2C_Z)L_C}$, the circuit Laplacian (7) exactly recovers the TB Hamiltonian by the following one-to-one correspondence: $-\omega_0 C_A \leftrightarrow t_a$, $-\omega_0 C_B \leftrightarrow t_b$, and $-\omega_0 C_Z \leftrightarrow t_z$. To explore the square-root topological semimetal phase, we set $C_A = C_B/2 = 0.5$ nF, $C_Z = 0.5$ nF and $L_A = 30$ μH, $L_B = 7.5$ μH, and $L_C = 18$ μH in the following calculations, if not stated otherwise.

To facilitate the detection of the hinge states through a direct two-point impedance measurement[39], we connect a grounded inductor $L_G = 22$ μH to all nodes to move the hinge modes to the zero admittance without modifying their wave functions[6]. By measuring the impedance, one can precisely characterize the wave function of the zero-admittance hinge states in circuit[6,39]. Figure 2b exhibits the corresponding admittance spectrum, where the red, blue, and black dots represent the hinge, surface, and bulk states, respectively. One can see the three-fold degeneracy of the in-gap hinge states due to the C_3 symmetry and generalized chiral symmetry[6]. In addition, the time reversal symmetry dictates the bulk/surface states being singlet or double-degenerate. The spatial distributions of each mode are plotted in Fig. 2c–e, from which one can straightforwardly distinguish them.

The photograph of 3D LC electric circuits fabricated on a printed circuit board (PCB) is displayed in Methods. Our circuit is designed
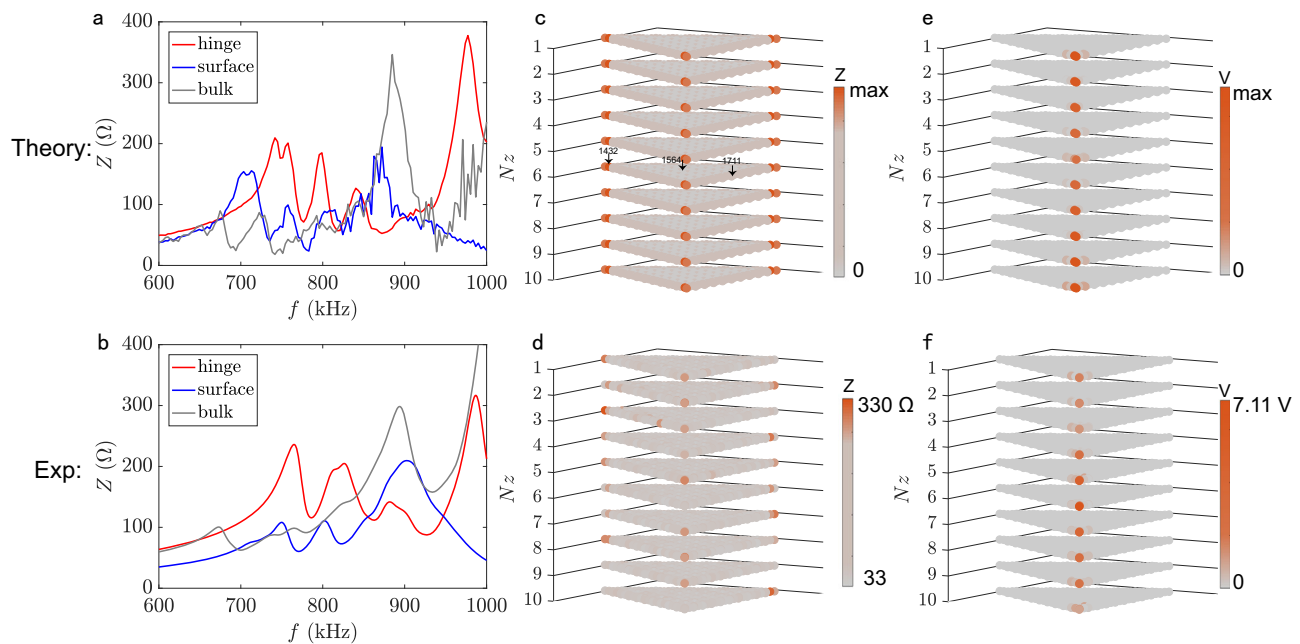
Fig. 3 | Impedances spectra, impedances and voltage distributions.
a Theoretical impedance versus the driving frequency in a disordered circuit.
b Measured impedance as a function of the frequency. Calculated (**c**) and measured

(**d**) impedance distribution of hinge state over the system. Hinge-state voltage distribution in theory (**e**) and experiment (**f**).

by Altium Designer. The connection between different layers of the circuit boards is through flexible flat cable. We choose electric elements $C_A = C_B/2 = 0.5$ nF, $C_Z = 0.5$ nF and $L_A = 30$ μH, $L_B = 7.5$ μH, $L_C = 18$ μH and $L_G = 22$ μH, the same as those for theoretical computations above, but with a practical 2% tolerance. The resonant frequency is then $f_c = 1/(2\pi\sqrt{3C_AL_A}) = 755$ kHz. We first measure the impedance between three representative nodes and the ground as a function of the exciting frequency with the impedance analyzer (Keysight E4990A). Experimental results are shown in Fig. 3b, which agree well with theoretical calculations plotted in Fig. 3a. Here we select the 1432nd, 1564th, and 1711st nodes (specified in Fig. 3c) to characterize the properties of the hinge, surface, and bulk states, respectively. We then measure the spatial distribution of the impedance and voltage over the circuit (Fig. 3d, f), which compare reasonably well with the theoretical results plotted in Fig. 3c, e.

To characterize the hinge states more carefully, we project the dispersion to the k_z axis, as shown by the color map in Fig. 4a. In theoretical calculations, one can conveniently set different admittances j_n and analyze the spectrum. For circuit experiments, we can shift an arbitrary admittance to zero by adjusting the value of L_G. This is what we have done for measuring the hinge states. To demonstrate another experimental technique, we, alternatively, tune the frequency to measure the Fermi-arc surface state with the same circuit structure. Fortunately, by mapping Kirchhoff's law to the Schrödinger equation in circuit[40,41], we obtain the frequency dispersion (see Supplementary Note 5) that significantly facilitates our experimental measurements. A continuous variation of the frequency can be seen as an adiabatic transformation of our model, with everything else kept constant. Experimentally, we impose a voltage source in the middle of one hinge of the circuits, and scan the voltage distribution along the hinge. Specifically, we input a signal $v_s(t) = 5\sin(\omega t)$ V at a hinge node with the arbitrary function generator (GW AFG-3022), and then collect the voltage $v(\omega, z)$ with frequency $f = \omega/(2\pi)$ ranging from 500 kHz to 1600 kHz by using the oscilloscope (Keysight MSOX3024A). We perform the Fourier transformation on the $v(\omega, z)$ and obtain the projected dispersion along the k_z direction, shown by the color map in Fig. 4b. It can be seen that the hinge states connect

two Weyl points at a resonant frequency around 860 kHz and 1441 kHz, which perfectly agrees with the simulation results marked by the solid red circles.

Furthermore, it is known that the "Fermi arc" surface state is an unique feature of Weyl semimetals. The Weyl points emerge at $j_n = \pm 0.004082$ Ω^{-1} (shown in Fig. 4a), which corresponds to frequencies $f = 835$ and 1441 kHz in Fig. 4b. However, $f = 1441$ kHz deviates a lot from the working frequency of our selected electric components, because the component values suffer a drastic change (the values of electric components depend on the frequency). So, we only consider $f = 835$ kHz to display the complete "Fermi arc" (Fig. 4d). Figure 4c shows the "Fermi arc" surface dispersion at $j_n = 0.004082$ Ω^{-1}. Figure 4d shows the "Fermi arc" surface dispersion at $f = 835$ kHz. Here, we determine k_x by $k_x = 2\pi m/N$, with $m = 1, 2, 3, \ldots N - 1$, and N being the number of grid points in the $\hat{x}$ direction. The geometry used for the experimental measurement in Fig. 4d is a side face of the triple prism. We consider periodic boundary condition along $\hat{z}$ direction and open boundary condition along both $\hat{x}$ and $\hat{y}$ directions. The color map represents the measured data and the white circles denote the simulated equal-admittance contour, whereas the hollow and solid dots denote the projections of Weyl points with opposite topological charges $+1$ and -1, respectively. Our experiment therefore unambiguously supports the bulk-hinge correspondence and identifies the emergence of SHOWS.

Discussion

To summarize, we proposed a TB model of the SHOWS and constructed it in 3D double-helix stacked LC circuits. Through the impedance and voltage measurements, we directly observed both the 1D prismatic states and the 2D "Fermi arc" surface states connecting the projection of Weyl points on the arris and side surface respectively, the fingerprint of SHOWS. Comparing with the normal Weyl semimetal[18], the SHOWS supports robust hinge states, besides the arc surface states. The emergence of Weyl pairs in SHOWS with both positive and negative energies marks its difference from the conventional higher-order Weyl semimetals[22–29]. One of the parent sublattices, i.e., the honeycomb lattice, originally does not support any hinge states or flat-
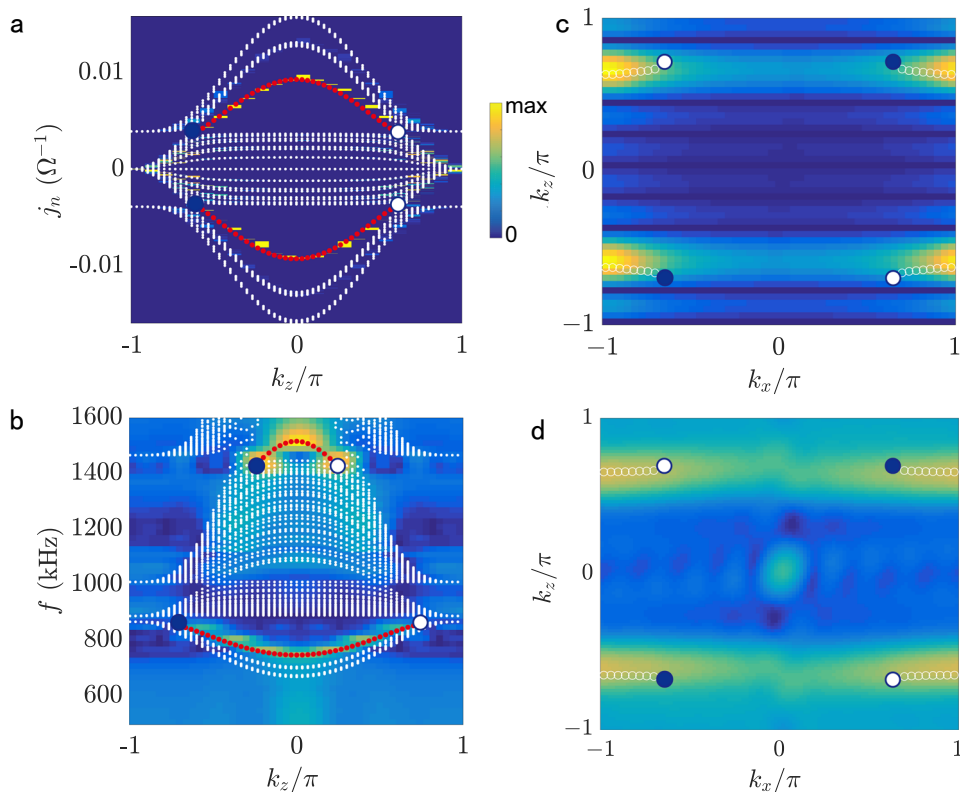
Fig. 4 | Hinge states and Fermi arcs. a The projected admittances along k_z axis. **b** Hinge-state dispersion connecting the projection of the Weyl points on k_z axis. The red dots and the color map in **a** and **b** represent the theory and experimental hinge spectrum, respectively. **c** The numerical "Fermi arc" of the surface states at $j_n = 0.004082\,\Omega^{-1}$, connecting the projections of the Weyl points on k_x-k_z surface. **d** "Fermi arc" of the surface states at 835 kHz. The color map and the white circles represent the experimental and theoretical results, respectively.
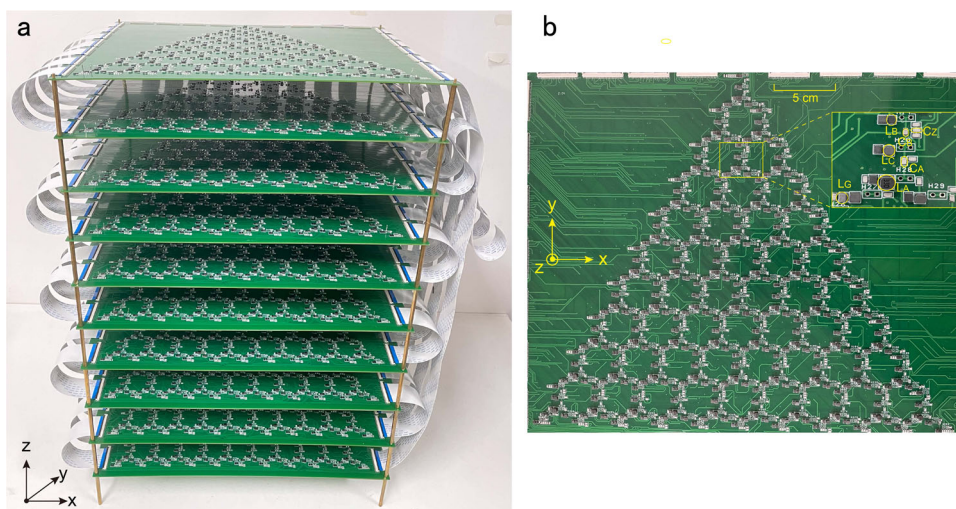
Fig. 5 | The printed circuit board. Side **a** and top **b** view of the printed circuit board in experiment.

band states. The square-root operator, however, makes it inherit these exotic states from the other parent sublattice. When the square-root operation is applied, the spectra of the blocks are necessarily degenerate[44] and the degenerate boundary modes of the honeycomb lattice are not topological but impurity states, stemming from onsite energy offsets at the boundary nodes[11]. In the present model, by adjusting the interlayer hopping t_z to be breathing, we envision the emergence of third-order corner states[45].

From the application perspective, both hinge states and surface states can be used to design robust solid-state devices. For

example, one can transmit the signal with extremely low loss[46] and devise the multiplexing[47] and imaging[48] with these topologically boundary modes. Recently, it is shown that the topological LC circuit can be fully integrated by complementary metal-oxide-semiconductor (CMOS) technology[49,50], which may solve the outstanding challenges met in the chip industry. Our findings may stimulate the effort in the broad physics and materials community to look for real materials that support SHOWS, since we have provided a rather general framework to construct the Hamiltonian. It can be utilized to conduct electric charge with faster velocity[17,51]. Since Weyl particles are

Table 1 | Electric elements used in experiments

	Electric elements	Mean value	Tolerance
C_A	FH 0805 (50 V)	0.5 nF	± 2%
C_B	Walsin 0805 (50 V)	1 nF	± 2%
C_Z	FH 0805 (50 V)	0.5 nF	± 2%
L_A	SXN 4040 (1.1 A)	30 μH	± 2%
L_B	Cjiang 2520 (680 mA)	7.5 μH	± 2%
L_C	Cjiang 3030 (560 mA)	18 μH	± 2%
L_G	FH 2521 (380 mA)	22 μH	± 2%

The capacitors are produced by FH and Walsin company, with the 0805 package. The inductors belong to the low-resistance power surface-mount devices, produced by SXN, Cjiang, and FH company, with the 4040, 2520, 3030, and 2521 package. The tolerance of circuit elements are selected within 2% manually.

topologically protected from scattering[19,20], they could be useful in quantum information science. One may use the square-root method to explore many interesting new ideas for further study. For example, in electrical circuits, one may discover the enchanting phenomenon with square-root operations in higher dimensions, e.g., four-dimension (4D)[52]. One may apply square-root operation to the Floquet TIs or semimetals, sustained by time-dependent periodic Hamiltonians[50,53]. Beyond the square-root, one can generalize the approach to the 2^n-root weak, Chern, and higher-order topological insulators, and 2^n-root topological semimetals[11,15]. Our results thus pave the way to realizing the square-root higher-order topological states in electric circuits, and may inspire the exploration in other solid-state systems, such as cold atoms, photonic crystals, and elastic lattices.

Methods

Circuit Laplacians and PCB images in experiments

The circuit dynamics at frequency ω obeys Kirchhoff's law $I_a(\omega) = \sum_b J_{ab}(\omega)V_b(\omega)$, with I_a the external current flowing into node a, V_b the voltage of node b, and $J_{ab}(\omega)$ being the circuit Laplacian

$$J_{ab}(\omega) = i\mathcal{H}_{ab}(\omega) = i\omega\left[-C_{ab} + \delta_{ab}\left(\sum_n C_{an} - \frac{1}{\omega^2 L_a}\right)\right], \qquad (8)$$

where C_{ab} is the capacitance between a and b nodes, L_a is the grounding inductance of node a, and the sum is taken over all nearest-neighboring nodes. For a finite circuit, the Laplacian of the circuit can be written as Eq. 7 in the main text. Considering the resonance condition $\omega = \omega_0$, one can obtain all eigenvalues j_n (admittances) and eigenfunctions ψ_n ($n = 1, 2, ..., \mathcal{N}$). The geometry used for the experimental is a triangular prism shown in Fig. 5a. The geometry used for the theoretical calculations in Fig. 4a, b is also a triangular prism (open boundary condition in $k_x - k_y$ plane and periodic boundary condition along k_z direction) including 286 nodes in each layer. The geometry used for the theoretical results in Fig. 4c, d, Supplementary Fig. 3a, Supplementary Fig. 4 and Supplementary Fig. 5 is a slab (open boundary condition along k_y direction and periodic boundary condition along both $\hat{x}$ and $\hat{z}$ directions) containing 155 nodes.

Table 1 lists electric elements used in experiments.

In the calculation of Fig. 2 in the main text, we consider the ideal situation that all inductors and capacitors have no loss and disorder. Considering the practical loss and tolerance of capacitors and inductors, we introduced 2% disorder to each capacitor and inductor in theoretical calculations thereafter. In experiments, we stacked ten identical 2D printed circuit boards (PCBs) along the $\hat{z}$ direction, as shown in Fig. 5a. Figure 5b shows the top view of the PCB with the inset zooming in the design details of the electrical circuit.

Data availability

The data that support the plots within this paper and other findings of this study have been deposited in the Zenodo database : https://doi.org/10.5281/zenodo.6976420.

Code availability

We used the commercial software MATLAB to perform the numerical calculations. Requests for the computation details can be addressed to the corresponding author.

References

1. Dirac, P. A. M. The quantum theory of the electron. *Proc. R. Soc. Lond. A* **117**, 610 (1928).
2. Greiner, W. *Relativistic Quantum Mechanics: Wave Equations* (Springer Verlag, 2003).
3. Anderson, C. D. The positive electron. *Phys. Rev.* **43**, 491 (1933).
4. Arkinstall, J., Teimourpour, M.-H., Feng, L., El-Ganainy, R. & Schomerus, H. Topological tight-binding models from nontrivial square roots. *Phys. Rev. B* **95**, 165109 (2017).
5. Kremer, M. et al. A square-root topological insulator with non-quantized indices realized with photonic Aharonov-Bohm cages. *Nat. Commun.* **11**, 907 (2020).
6. Song, L., Yang, H., Cao, Y. & Yan, P. Realization of the square-root higher-order topological insulator in electric circuits. *Nano Lett.* **20**, 7566–7571 (2020).
7. Mizoguchi, T., Kuno, Y. & Hatsugai, Y. Square-root higher-order topological insulator on a decorated honeycomb lattice. *Phys. Rev. A* **104**, 029906 (2021).
8. Yan, M. et al. Acoustic square-root topological states. *Phys. Rev. B* **102**, 180102 (2020).
9. Yan, W. et al. Realization of second-order photonic square-root topological insulators. *ACS Photonics* **8**, 3308–3314 (2021).
10. Jung, M., Yu, Y. & Shvets, G. Exact higher-order bulk-boundary correspondence of corner-localized states. *Phys. Rev. B* **104**, 195437 (2021).
11. Marques, A. M. & Dias, R. G. 2^n-root weak, Chern, and higher-order topological insulators, and 2^n-root topological semimetals. *Phys. Rev. B* **104**, 165410 (2021).
12. Wu, H., Wei, G., Liu, Z. & Xiao, J.-J. Square-root topological state of coupled plasmonic nanoparticles in a decorated Su-Schrieffer-Heeger lattice. *Opt. Lett.* **46**, 4256–4259 (2021).
13. Dias, R. G. & Marques, A. M. Matryoshka approach to sine-cosine topological models. *Phys. Rev. B* **103**, 245112 (2021).
14. Yoshida, T., Mizoguchi, T., Kuno, Y. & Hatsugai, Y. Square-root topological phase with time-reversal and particle-hole symmetry. *Phys. Rev. B* **103**, 235130 (2021).
15. Marques, A. M., Madail, L. & Dias, R. G. One-dimensional 2^n-root topological insulators and superconductors. *Phys. Rev. B* **103**, 235425 (2021).
16. Kang, J. et al. Observation of square-root higher-order topological states in photonic waveguide arrays. *arXiv* https://doi.org/10.48550/arXiv.2109.00879 (2021).
17. Weyl, H. Elektron und gravitation. I. *Z. Phys.* **56**, 330–352 (1929).
18. Wan, X., Turner, A. M., Vishwanath, A. & Savrasov, S. Y. Topological semimetal and Fermi-arc surface states in the electronic structure of pyrochlore iridates. *Phys. Rev. B* **83**, 205101 (2011).
19. Xu, S.-Y. et al. Discovery of a Weyl fermion semimetal and topological Fermi arcs. *Science* **349**, 613–617 (2015).
20. Lu, L. Experimental observationn of Weyl points. *Science* **349**, 622–624 (2015).
21. Lv, B. Q. et al. Experimental discovery of Weyl Semimetal TaAs. *Phys. Rev. X* **5**, 031013 (2015).
22. Wang, H.-X., Lin, Z.-K., Jiang, B., Guo, G.-Y. & Jiang, J. Higher-order Weyl semimetals. *Phys. Rev. Lett.* **125**, 146401 (2020).

23. Rui, W. B. et al. Higher-order Weyl superconductors with anisotropic Weyl-point connectivity. *Phys. Rev. B* **103**, 184510 (2021).
24. Rui, W. B. et al. Intertwined Weyl phases emergent from higher-order topology and unconventional Weyl fermions via crystalline symmetry. *npj Quantum Mater.* **7**, 15 (2022).
25. Roy, B. Antiunitary symmetry protected higher-order topological phases. *Phys. Rev. Res.* **1**, 032048(R) (2022).
26. Ghorashi, S. A. A., Li, T. & Hughes, T. L. Higher-order Weyl semi-metals. *Phys. Rev. Lett.* **125**, 266804 (2020).
27. Wei, Q., Zhang, X., Deng, W., Lu, J. & Jia, S. Higher-order topological semimetal in acoustic crystals. *Nat. Mater.* **20**, 812–817 (2021).
28. Qiu, H., Xiao, M., Zhang, F. & Qiu, C. Higher-order dirac Sonic crystals. *Phys. Rev. Lett.* **127**, 146601 (2021).
29. Luo, L. et al. Observation of a phononic higher-order Weyl semi-metal. *Nat. Mater.* **20**, 794–799 (2021).
30. Mizoguchi, T., Yoshida, T. & Hatsugai, Y. Square-root topological semimetals. *Phys. Rev. B* **103**, 045136 (2021).
31. van Miert, G. & Ortix, C. On the topological immunity of corner states in two-dimensional crystalline insulators. *npj Quant. Mater.* **5**, 63 (2020).
32. Dong, J., Juričić, V. & Roy, B. Topolectric circuits: theory and construction. *Phys. Rev. Res.* **3**, 023056 (2021).
33. Luo, K., Yu, R. & Weng, H. Topological nodal states in circuit lattice. *Research* **2018**, 6793752 (2018).
34. Lu, Y. et al. Probing the berry curvature and fermi arcs of a Weyl circuit. *Phys. Rev. B* **99**, 020302(R) (2019).
35. Yang, Y.-B., Qin, T., Deng, D.-L., Duan, L.-M. & Xu, Y. Topological amorphous metals. *Phys. Rev. Lett.* **123**, 076401 (2019).
36. Rafi-Ul-Islam, S. M., Bin Siu, Z. & Jalil, M. B. A. Topoelectrical circuit realization of a Weyl semimetal heterojunction. *Commun. Phys.* **3**, 72 (2020).
37. Lee, C. H. et al. Imaging nodal knots in momentum space through topolectrical circuits. *Nat. Commun.* **11**, 4385 (2020).
38. Li, R. et al. Ideal type-II Weyl points in topological circuits. *Nat. Sci. Rev.* **8**, nwaa192 (2020).
39. Yang, H., Li, Z.-X., Liu, Y., Cao, Y. & Yan, P. Observation of symmetry-protected zero modes in topolectrical circuits. *Phys. Rev. Res.* **2**, 022028(R) (2020).
40. Hofmann, T., Helbig, T., Lee, C. H., Greiter, M. & Thomale, R. Chiral vgoltage propagation and calibration in a topolectrical chern circuit. *Phys. Rev. Lett.* **122**, 247702 (2019).
41. Yang, H., Song, L., Cao, Y., Wang, X. R. & Yan, P. Experimental observation of edge-dependent quantum pseudospin Hall effect. *Phys. Rev. B* **104**, 235427 (2021).
42. Rafi-Ul-Islam, S. M., Siu, Z. B., Sahin, H., Lee, C. H. & Jali, M. B. A. Unconventional node voltage accumulation in generalized topolectrical circuits with multiple asymmetric couplings. *arXiv* https://doi.org/10.48550/arXiv.2108.01366 (2021).
43. Yang, H., Song, L., Cao, Y., Wang, X. R. & Yan, P. Experimental realization of two-dimensional weak topological insulators. *Nano Lett.* **22**, 3125–3132 (2022).
44. Ezawa, M. Systematic construction of square-root topological insulators and superconductors. *Phys. Rev. Res.* **2**, 033397 (2020).
45. Geng, Z.-G. et al. Square-root-like higher-order topological states in three-dimensional sonic crystals. *J. Phys. Condens. Matter* **34**, 104001 (2022).
46. Wei, Q. et al. 3D hinge transport in acoustic higher-order topological insulators. *Phys. Rev. Lett.* **127**, 255501 (2021).
47. Ni, X., Xiao, Z., Khanikaev, A. B. & Alù, A. Robust multiplexing with topolectrical higher-order chern insulators. *Phys. Rev. Appl.* **13**, 064031 (2020).
48. Zhang, Z., Long, H., Liu, X. & Christensen, J. Deep-subwavelength holey acoustic second-order topological insulators. *Adv. Mater.* **31**, 1904682 (2019).
49. Cao, W. et al. Fully integrated parity-time-symmetric electronics. *Nat. Nanotechnol.* **17**, 262–268 (2022).
50. Nagulu, A. et al. Chip-scale floquet topological insulators for 5G wireless systems. *Nat. Electron.* **5**, 300–309 (2022).
51. Shekhar, C. et al. Extremely large magnetoresistance and ultrahigh mobility in the topological Weyl semimetal candidate NbP. *Nat. Phys.* **11**, 645–649 (2015).
52. Yu, R., Zhao, Y. X. & Schnyder, A. P. 4D spinless topological insulator in a periodic electric circuit. *Natl Sci. Rev.* **7**, 1288–1295 (2020).
53. Bomantara, R. W. Square-root Floquet topological phases and time crystals. *arXiv* https://doi.org/10.48550/arXiv.2111.14327 (2021).

Acknowledgements

Author contributions

P.Y. conceived the idea and contributed to the project design. L.S. and H.Y. designed the circuits and performed the measurements. L.S. developed the theory and wrote the manuscript. L.S., H.Y., Y.C. and P.Y. discussed the results and revised the manuscript.

Competing interests

The authors declare no competing interests.

Additional information

Supplementary information The online version contains supplementary material available at https://doi.org/10.1038/s41467-022-33306-9.

Correspondence and requests for materials should be addressed to Peng Yan.

Peer review information *Nature Communications* thanks Anselmo Marques and the other, anonymous, reviewer(s) for their contribution to the peer review of this work. Peer reviewer reports are available.

Reprints and permission information is available at http://www.nature.com/reprints

Publisher's note Springer Nature remains neutral with regard to jurisdictional claims in published maps and institutional affiliations.